Optical tweezers combined with FRET tension sensor reveal force-dependent vinculin dynamics

Condensed running title (max 40 characters): Vinculin tension sensor under force

Authors

Camille Dubois[1], Rick I. Cohen[2,3], Nada N. Boustany[2,*], Nathalie Westbrook[1,*]

1 Université Paris-Saclay, Institut d'Optique Graduate School, CNRS, Laboratoire Charles Fabry, Palaiseau, France
2 Rutgers University, Dept. of Biomedical Engineering, Piscataway, New Jersey, United States
3 Present address: TheWell Bioscience Inc., Monmouth Junction, New Jersey, United States
* Correspondence: nathalie.westbrook@institutoptique.fr, nboustan@rutgers.edu

Abstract (max 300 words)

Methods to visualize and quantify the molecular responses of cells to local forces exerted at adhesions are crucial to elucidate how physical forces control cellular behavior. Of the many proteins involved in focal adhesions, vinculin plays a key role in mediating force-sensitive processes. Here, we combine optical tweezers and Förster resonance energy transfer (FRET) microscopy to measure the intensity and FRET efficiency of the vinculin tension sensor, VinTS, in response to a force. Fibroblasts expressing VinTS formed adhesions on fibronectin-coated, 3µm-diameter, polystyrene beads, which were subjected to an optical trap with adjustable stiffness up to 0.26 pN/nm. After 5 min, the mean bead displacement was ~200nm in all trapping conditions inducing counteracting forces in the 10-100pN range. In response to the optical trap, vinculin recruitment and tension increased as a function of time. The mean increase in vinculin tension (1-2% decrease in absolute FRET efficiency) attained after 5 min was not significantly different at the different trapping conditions. However, vinculin recruitment was significantly higher at the higher trap stiffness with up to 35% increase in intensity at 0.26 pN/nm compared with <10% increase at 0.13 pN/nm, and an average 3% decrease in intensity for untrapped beads. The increase in vinculin intensity was correlated with the decrease in FRET efficiency at 0.26 pN/nm but not at lower stiffness. Thus, the presence of the high stiffness optical trap over 5 min appears to induce a positive correlation between vinculin recruitment and vinculin tension. In a few instances, vinculin puncta migrated a few microns away from the bead exceeding the bead's movement speed while experiencing an increase in both vinculin intensity and tension. Taken together, the results suggest that combining an optical trap with vinculin tension measurements uncovers novel vinculin dynamics in the presence of a force.

Statement of significance (max 120 words)

A fully calibrated system combining optical tweezers with FRET microscopy is developed and used to measure vinculin tension and recruitment in response to a force. The results demonstrate a correlation between vinculin recruitment and vinculin tension when the cell's adhesion force is counteracted for 5 min by an optical trap stiffness of 0.26 pN/nm. This response was absent when a lower trap stiffness (0.13 pN/nm) was used or in the absence of the optical trap. Such dynamic measurements, enabled by the techniques presented in this paper, can help elucidate the mechanisms by which cells sense physical forces and the properties of proteins, such as vinculin, which play a fundamental role in cellular behaviors involving tissue growth and repair.

1. Introduction

Cell signaling via mechanotransduction is the process by which cells sense and respond to physical forces. Mechanotransduction involving the actin cytoskeleton enables the physiological execution of fundamental dynamic cellular behaviors such as cell movement and cell migration, which are necessary for tissue organization and morphological development (1,2). These processes also play an important role in pathophysiological conditions including wound healing, tissue repair, tumor growth and metastasis (3).

Tension forces within cells, generated by actin polymerization at the leading edge or by actin-myosin contraction, are mediated by the formation of focal adhesions and adherens junctions (4-7) connecting the cell to the extra-cellular matrix (ECM), or to adjacent neighboring cells, respectively. Adhesion complexes initiated when integrins bind to the ECM or when cadherins of neighboring cells bind together, mature under mechanical load into stable adhesions through the activation and recruitment of additional proteins (8).

More than 150 proteins are known to participate in the integrin or cadherin adhesome (9,10). Although the processes by which these proteins are activated and recruited have not been completely elucidated, recent work has revealed some key mechanisms. One such mechanism is stretch induced signaling, where tension forces expose cryptic binding sites, altering protein interactions and their downstream functions. For example, talin, a protein linking integrins and the actin cytoskeleton, exposes vinculin binding sites when under tension (11,12). Similarly, at cadherin mediated cell-cell adhesions, α-catenin, linking cadherins and actin, exposes vinculin binding sites when stretched (13). Thus, vinculin is specifically recruited to adhesions in a tension-driven manner (14). Activation of vinculin releases the autoinhibitory interaction between vinculin's head and tail domains and unveils talin and actin binding sites (15-17) as well as a binding site allowing dimerization of the vinculin tail leading to actin bundling (18,19) which is necessary for strengthening adhesions in response to a force (20). Tension across vinculin itself leads to the recruitment of additional components, such as zyxin (21), further strengthening the adhesion complex. In addition to proteins that structurally reinforce the adhesion, protein kinases including Src, FAK, and Rho, also present within the adhesion complex, get activated under tension. These kinases phosphorylate downstream effectors, which can then control protein synthesis, cytoskeletal structure and cell growth (22). Developing methods to visualize or quantify the molecular responses of cells to local forces exerted at adhesion sites is crucial to advance our understanding of how physical forces control cellular behavior.

Various tools and methodologies have been developed to study the effect of forces on the formation and dynamics of adhesion complexes. Techniques employed to mechanically perturb living cells include varying substrate stiffness (23-31), stretching the substrate (14,32) or applying fluid shear stress to the culture (33). External forces can be applied locally to cells via suction pipets (23,34), optical tweezers (32,35-39) or integrin-coated magnetic beads (40). Disruption of internal cellular forces can also be induced by disrupting actin stress fibers or blocking acto-myosin contractility (14,23,26,34,41-43). Traction force microscopy (28,44,45) and deformable patterned substrates (23,30,46,47) may be used to measure the forces imparted by the cell at focal adhesions while fluorescence microscopy is applied to observe protein recruitment (26,36,48), focal adhesion growth (26,43,49), focal adhesion strength (30,48), adhesion reinforcement (32,50), protein kinase activation (39), YAP nuclear translocation (32), protein dynamics and actin flow (30,32,51,52), in response to specific mechanical perturbations. Molecular tension probes based on Förster Resonance Energy Transfer (FRET) have added the ability to quantify internal forces on the proteins within focal adhesions on the pN scale, and to do so in a dynamic way (53,54). Mechanical models were also developed to explain protein dynamics at cell adhesions and elucidate cellular behaviors such as migration or sensitivity to the stiffness of the extracellular matrix (24,25,55-57).

Optical tweezers allow the application of controlled, precise, localized forces while measuring the cell's reaction force with high temporal resolution. They have been used to study the growth and maturation of focal adhesions as a function of force and the role of vinculin in this process (35-37). In addition, the ability to control the loading rate using optical tweezers was used to study the frequency response of adhesion properties and a better characterization of focal adhesion dynamics (32). Optical tweezers were combined with FRET microscopy to demonstrate Src activation in response to mechanical force (39) and an instrument design incorporating optical tweezers with FRET microscopy of F-actin and α-actinin tension probes was proposed (58). Here, we demonstrate, for the first time, a setup combining optical tweezers with fluorescence FRET measurements of the vinculin tension sensor (VinTS) in living cells.

Our fluorescence FRET setup, which is based on a wide-field sensitized emission measurement and capable of quantifying VinTS FRET efficiency at the focal adhesions of living cells (59), is combined with optical tweezers passing through the same microscope objective. The optical tweezers are utilized to counteract and measure the force applied by a cell on a functionalized microbead attached to its surface while acquiring the FRET efficiency. Thus, the instrument enables directly measuring changes in vinculin intensity and tension in response to cell force. We present results demonstrating how this combination of measurements may be used to uncover vinculin dynamics in the presence of force.

2. Materials and methods

2.1. Sample preparation

2.1.1. Beads

Carboxylated polystyrene beads of 3µm or 6µm diameter from Polysciences were functionalized with fibronectin (FN) (Sigma-Aldrich F0895). For this coating, 10µL of stock beads were incubated with 20µg of poly-lysine in 100µL of PBS for 1h at room temperature, then washed twice with Phosphate-Buffered Saline solution (PBS). The 3µm beads were then incubated with 2µg of FN, and the 6 µm beads with 4µg of FN, both in 100µL of PBS, for 1h at room temperature. Beads were washed again

twice with PBS and resuspended in 100µL of PBS. Fresh beads were prepared a few days before each experiment.

2.1.2. Lentivirus packaging

All procedures were carried out using Biosafety Level 2+ procedures, sterile solutions, and materials unless indicated. The pRRL-VinTS lentivirus vector (60) was generated in HEK293FT cells using protocols with a second-generation plasmid mixture as described previously (61). Details are provided in the Supplementary Methods.

2.1.3. Lentivirus transduction of hTERT-Immortalized Human Foreskin Fibroblasts

Primary normal human neonatal skin fibroblasts (HDFn) from LifeLine Cell Technology (FC-0001) previously immortalized using a pBM14 based vector (62) containing the Open Reading Frame of hTERT (human telomerase reverse transcriptase) (63) were transduced with the 100x concentrated lentivirus containing VinTS. Briefly, subconfluent fibroblast cultures grown in serum medium were rinsed with DMEM/F12 base medium and switched to Optimem containing 10 µg/mL of protamine sulfate. After 1 hour, the lentivirus was added at 1:50, 1:100, and 1:200 dilution. The following day the medium was removed and replaced with a standard serum medium. The expression of VinTS was monitored by microscopy 48 hours post transduction. The 1:50 and 1:100 dilutions resulted in successfully transduced fibroblasts which were subcultured using routine techniques for following tension measurement experiments.

2.1.4. Cell culture

The transduced fibroblasts expressing VinTS were maintained at 37°C, 5% CO2 in high glucose Dulbecco's Modified Eagle's Medium supplemented with 10% fetal bovine serum, 1% penicillin/streptomycin, and 1% L-glutamine (all from Gibco). Cells were seeded on 25mm diameter glass coverslips (1.5H Marienfeld Superior), previously cleaned with nitric acid, rinsed 10 times with sterile water, then incubated 1min in methanol, and air dried. Cells were plated at 20,000/cm^2 if imaged the next day or at 10,000-15,000/cm^2 if imaged 2-3 days after plating. Before imaging, cells were mounted in Live Cell Imaging Solution (Invitrogen) and incubated with functionalized beads at 37°C for 45 min, a time long enough for the beads to land on the cells and for focal adhesions to be created around the beads but not too long for internalization to occur. The beads that formed focal adhesions, on which our experiments were performed, were typically at the edge of the cell.

2.2. Optical setup

2.2.1. FRET image acquisition

The fluorescence FRET microscopy setup is based on a wide-field sensitized-emission measurement shown in Fig.1 that has been previously described in (59). Briefly, it is composed of two LEDs : a blue LED filtered around 438/24 nm to excite the donor fluorophore mTFP1 and a green LED filtered around 520/15 nm to excite the acceptor mVenus. The illumination intensity of each LED in the sample plane can be adjusted independently. They are chosen based on the half-life of the fluorophores which are set to 150 s for mTFP1 (33.0 mW/mm^2 for LED D) and 40 s for mVenus (11.6 mW/mm^2 for LED A). Half-life of the two fluorophores as a function of illumination intensity is shown in Fig. S1. Fluorescence is collected through a microscope objective (Nikon Plan Fluor 100x, NA = 1.3, oil immersion) and the donor and acceptor emissions are detected simultaneously on two sCMOS cameras (Basler acA2040-55 µm, 2048 x 1536 pixels, 3.45 µm pixels, quantum efficiency 65% at 550

nm, cameras 1 and 2 in Fig. 1), one for the donor and one for the acceptor. An additional camera (camera 3 in Fig. 1) provides a phase contrast image of the sample. An acquisition is automated without any mechanical movement. A FRET acquisition sequence consists of 2 steps: donor is excited with LED D and two images are acquired simultaneously, IDD (Donor excitation and Donor detection) on camera 1 and IDA (Donor excitation and Acceptor detection) on camera 2. Then, the acceptor is directly excited with LED A and the IAA image (Acceptor excitation and Acceptor detection) is acquired on camera 2. All the exposure times are 2s.

2.2.2. FRET efficiency calculation

The three raw images are processed with a Matlab (The MathWorks Inc.) routine. First, each image is background corrected and flat-field corrected. Then, a registration procedure based on a transformation matrix allowing for translation, rotation and scaling is applied to the IDD image so that it matches pixel-by-pixel with the images taken on the other camera. Fluorescence signals coming from the cells are isolated from the background by thresholding. Fluorescence signals isolated and corrected from each image are called DD, DA and AA.

Bleedthrough between channels was previously measured with cells transfected with acceptor only or donor only: the direct excitation of the acceptor when illuminating with the blue LED at 440 nm gave a ratio a = 0.169 between DA and AA and the donor fluorescence that passes through the acceptor detection channel gave a ratio d = 0.413 between DA and DD. These lead to a corrected FRET intensity: $Fc = DA - aAA - dDD$.

Using the calibration procedure described in (59), a G factor has been determined using cells expressing a standard FRET construct, TSMod, whose FRET efficiency has been measured independently by fluorescence lifetime microscopy (FLIM). Therefore, a quantitative FRET efficiency is given by :

$$Eff = \frac{\frac{Fc}{DD}}{G+\frac{Fc}{DD}} \qquad \text{with } G = 1.02$$

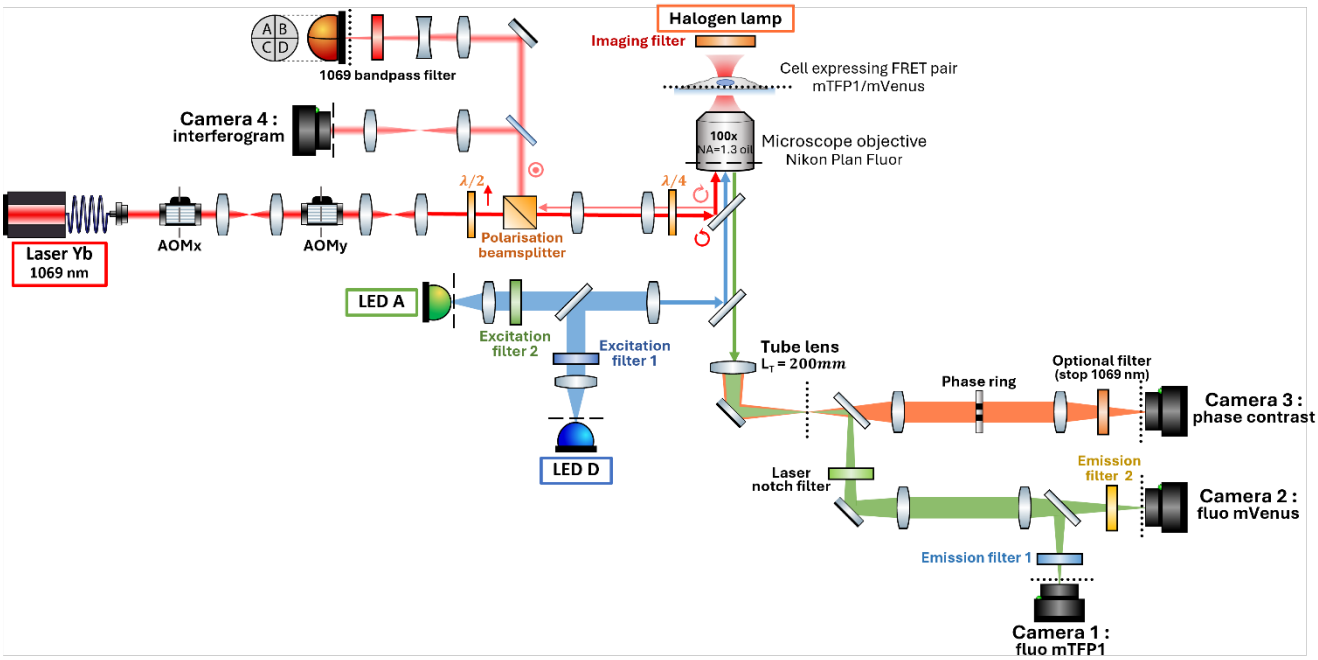

Figure 1 : *Experimental setup. Conjugate planes to the sample are indicated by dotted lines, those conjugate to the back focal plane of the objective by dashed lines. Filters used for FRET are 438/24 for Excitation 1, 520/15*

for Excitation 2, 482/35 for Emission 1, 562/40 for Emission 2. For more details on filters and dichroic mirrors, see (59).

2.2.3. Optical tweezer setup

The optical tweezer is based on an Ytterbium fiber laser at 1069 nm (Keopsys, TEM_{00}, linearly polarized) delivering up to 5 W at the output of the fiber. The beam is expanded by two afocal telescopes to cover the entrance pupil of the objective. The laser waist measured at the focal point is $\omega_{0,x}$ = 675nm and $\omega_{0,y}$ = 470nm.

Two orthogonal acousto-optic deflectors (AOD) (Intra Action Corp. DTD 274HA6) control the displacement of the trap in the transverse plane. The AODs are conjugate to the back-focal plane of the objective to get a pure translation of the trap in the sample plane.

The retroreflected light is separated from the incident beam by polarization and is imaged on a quadrant photodiode (QPD, SPOT-9DMI, OSI Optoelectronics). This detection samples the bead position at 62.5 kHz. Camera 4 in Fig. 1 is conjugate to the back-focal plane of the objective and images the interference pattern between the reflections at the bead bottom surface and at the top surface of the coverslip. Centering the rings in this interferogram is used to center precisely a bead at the center of the trap. The diameter of these rings also reports on the height of the bead with respect to the coverslip (64).

2.2.4. Optical tweezer calibration

2.2.4.1. Lateral position of the bead

Output signals of the QPD are normalized dimensionless signals and are converted into a metric position measurement using a conversion factor C. This factor is obtained using the step-response method : the trap is moved rapidly by a known distance in x and y and the QPD signal is measured as the bead comes back into the trap. The relative voltage of the QPD as a function of the step amplitude is linear over 400 nm around the trap center with a calibration factor $C = 1.0\ \frac{\Delta V}{V}/\mu m$ in both directions x and y (see Fig. S2).

2.2.4.2. Trap stiffness

The trap stiffness k is estimated from the motion of a bead trapped in water using the power spectrum analysis and the step-response method (64). The two methods are used in parallel on the same beads to ensure a reliable calibration. Stiffnesses obtained with the two methods are in close agreement and increase linearly with laser power with a slope of 0.71 pN/nm/W for the 3µm diameter beads used in the trapping experiments (see Fig. S3). We adjusted the trap stiffness using laser power, with a limit at 370 mW (at the entrance of the objective) to prevent sample damage. The trap stiffness was checked to be linear over the 400nm range of linearity of the QPD. Two power levels were used, 370mW or 180mW, corresponding to trap stiffnesses of 0.26 pN/nm and 0.13 pN/nm respectively, for 3 µm beads.

2.2.5. Trapping and image acquisition sequence

Fig. 2 shows the time sequence of our experiments. Once a bead with puncta of vinculin is identified, it is centered on the laser spot at low power, i.e. less than 10mW (Fig. 2a). The laser is rapidly turned to its nominal power, within less than 10 seconds (Fig. 2b). As the actin reorganisation within the cell displaces the bead along its membrane, the laser will induce a counteracting force on the bead (Fig. 2c). From the displacement value x of the bead from its initial position, we infer the

counteracting force of the optical trap on the bead as $F(t) = kx(t)$, where the stiffness k of the trap can be varied with laser power.

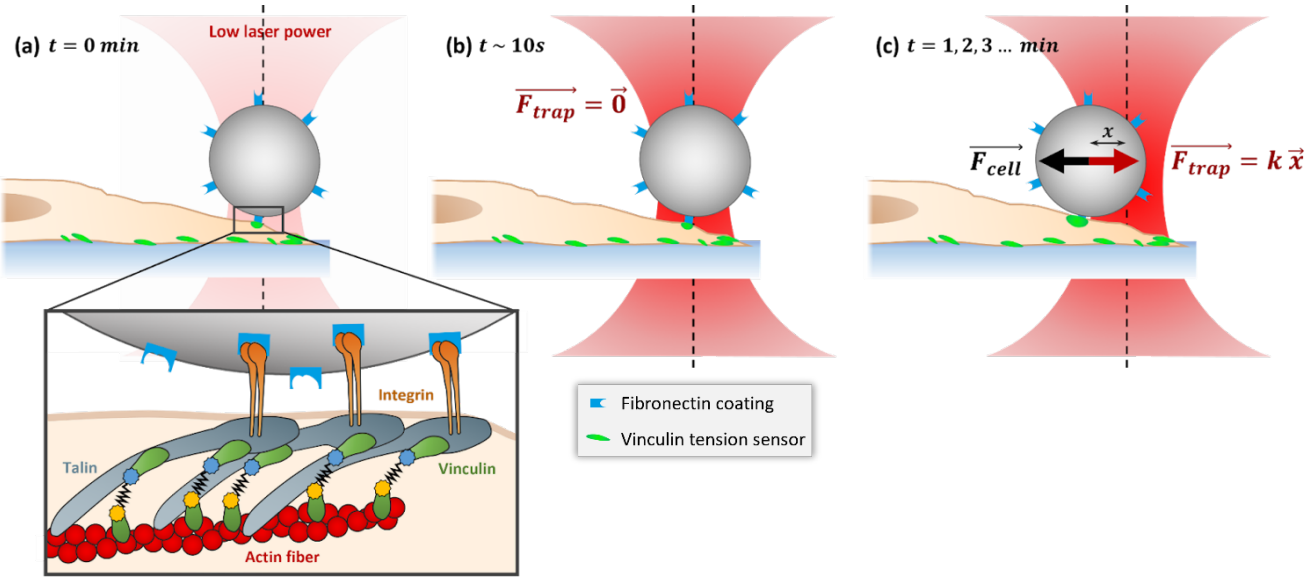

Figure 2 : *Principle of the application of the optical trap force on the cell. (a) A bead showing puncta of vinculin fluorescence is initially centered on the laser focus at low power using the interference pattern on Camera 4 (see Fig. 1). The first FRET sequence (consisting 3 images DA, DD and AA) is acquired at t=0 and is the first acquisition of the time-lapse. The inset shows the focal adhesion complex with the main proteins involved, and a FRET tension sensor inserted within vinculin, whose head and tail are bound to talin and actin, respectively. (b) The laser power is increased to the desired level immediately after the end of the first FRET acquisition. At that point, the bead is still centered so it does not experience a force from the trap. (c) As the cell displaces the bead, a force is exerted by the laser on the bead equal to $F = k\ x$ with k the trap stiffness and x the distance of the bead from its initial position. FRET sequences are recorded every minute.*

2.2.6. Image processing

The focal adhesions on the beads are extracted by manually drawing an annular region around the bead that includes the focal adhesions. This region of interest is adjusted for every acquisition: the annulus has a central radius between 40 and 55 pixels (corresponding to 1 to 1.4 µm) and a width between 20 and 35 pixels (i.e. 0.5 to 0.9 µm). The center of the annulus is shifted linearly over the time sequence to follow the bead. For each bead, focal adhesions are delimited angularly within this annulus. The number of focal adhesions per bead varies from 1 to 3, and their angular size ranges from 30 to 150° over all the focal adhesions analyzed. AA intensity and FRET efficiency values are averaged over each focal adhesion. Focal adhesions with initial AA intensity below 20 were excluded from the analyses as the signal-to-noise ratio below this intensity level results in a large uncertainty in the calculated FRET efficiency. To quantify the changes over time, the first image taken with the laser on (time t= 1min) is our reference in the analyses for the intensity and FRET efficiency measurements. The AA intensity values are normalized to the AA intensity at t= 1min, and FRET efficiency is reported over time as the difference between the FRET efficiency at time t and the FRET efficiency at t= 1min.

2.3. Confocal imaging

Confocal microscopy was used to visualize the focal adhesions with additional actin fluorescent labelling. Actin in fibroblasts expressing VinTS were labeled using CellLight Actin-RFP, BacMam 2.0 (Invitrogen C10583) following the manufacturer's protocol. On the next day, cells were incubated

with 6µm fibronectin coated beads for 45 min and then imaged. The mVenus within VinTS was excited with a laser at 514 nm and imaged in a bandwidth of 516-597nm. The RFP on actin was excited with a laser at 594nm and imaged in a bandwidth of 596 to 695 nm. Confocal microscopy was performed on a commercial laser scanning microscope (Zeiss 780 LSM) at the Rutgers BME High Resolution Microscopy Core Facility. 3D image rendering was performed using ImageJ Fiji software (65).

3. Results

3.1. Focal adhesion formation on beads

Fig.3 displays confocal images of a fibroblast cell, highlighting distinct puncta of vinculin around fibronectin-coated beads. These puncta are separate from the focal adhesions found at the surface of the coverslip. This separation is clearly illustrated in the x and y profiles presented alongside the right panel in Fig. 3a. The diffuse distribution of vinculin within the cell effectively delineates the cell membrane, confirming that the membrane surrounds the bead, as evidenced by the x and y profiles and the 3D renderings in Fig. 3b. Additionally, actin filaments, which are clearly visible on the coverslip surface, also emerge from at least two focal adhesion points on the bead. This pattern of focal adhesions linked to actin filaments was observed on many 6 µm beads (more examples in Fig. S4).

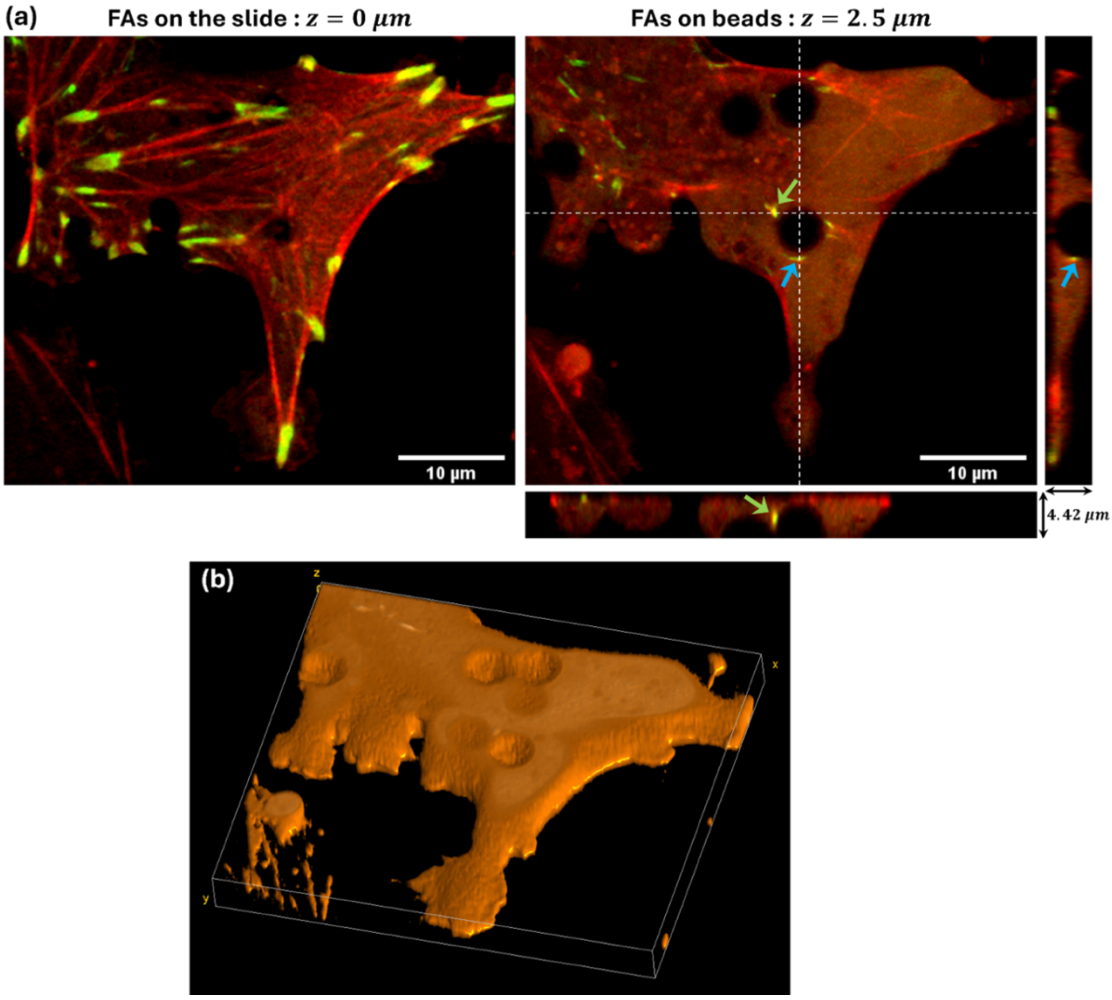

Figure 3 : *Confocal images of fibroblast cells after 45 min of incubation with 6µm beads coated with fibronectin. (a) Vinculin is marked using the tension sensor VinTS in green and actin is in red. Focal adhesions (FAs) on the coverslip are visible at $z = 0\ \mu m$ (left). At the height of the beads ($z = 2.5\ \mu m$), vinculin puncta are present on the surface of beads. Those FAs, marked by blue and green arrows are visible on the x and y-slices along the white dashed lines. (b) Volumetric reconstruction of the cell based on VinTS fluorescence, expressed over the whole cytoplasm. The spherical depressions correspond to the positions of the beads. The beads appear slightly embedded in the membrane.*

3.2. Intensity and FRET efficiency on beads as a function of time

A typical example of the data recorded for one bead is shown in Fig. 4. For higher stiffness in optical trapping (see stiffnesses for different bead diameters in Fig.S3) we used 3µm beads, which exhibit similar vinculin puncta as the 6µm beads. The phase contrast image in Fig. 4a shows that several beads are located on the cell, but one clearly presents accumulation of vinculin in the fluorescence image (Fig. 4b), corresponding to initial adhesions. We position this bead at the center of the trapping laser at low power. Fig. 4c shows the intensity (sum of the 3 images DD, DA and AA) and Fig. 4d the FRET efficiency around the bead as a function of time. On the intensity images, we clearly see that the two focal adhesion areas, on the right and left sides of the bead, both increase in intensity. Other examples of intensity images, recorded on different beads and cells, are shown in Fig. S5. The similar evolution of all focal adhesions on the same bead and the fact that they are subjected to the same optical trapping force justify that we averaged the values over all the focal adhesions for a given bead (between 1 and 3 FAs per bead).

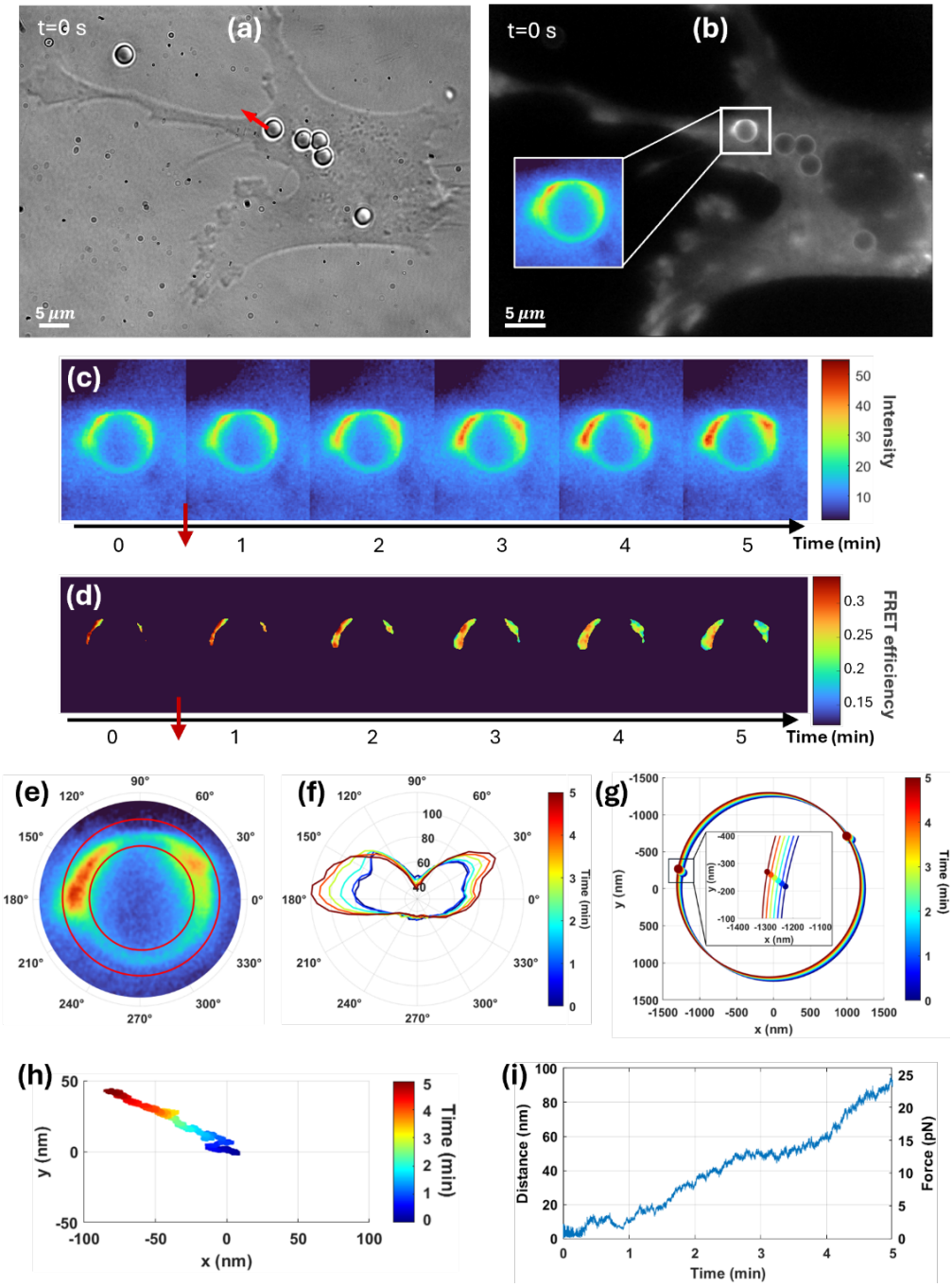

Figure 4 : *Signals recorded for one bead, shown as an example. Figures (a) and (b) are respectively the phase contrast and fluorescence images of a cell incubated with 3µm FN beads before the beginning of the laser trapping. This direction of motion of the bead is shown as a red arrow in panel (a). (c) Fluorescence images of the focal adhesions around the trapped bead recorded every minute after the laser is turned up to nominal power. The 3 images DD, DA and AA have been summed to increase contrast. AA intensity represents typically ⅓ of the total intensity. (d) Corresponding FRET efficiency images of the adhesions around the trapped bead. (e) Zoom on the fluorescence image at t=5 min, showing the annular region defined for the quantitative analysis of AA intensity and FRET efficiency. Two focal adhesions have been delimited on this bead, one at 30°±15° and 170°±20° (f) Polar plot of the AA intensity averaged over the width of the annular region shown in panel (e). Color codes for time. (g) Displacement of the annular region over the 5 recorded images: the circle segments represent the bead's position, and the dots the center of the focal adhesion, both as a function of time. (h) Trajectory of the bead recorded on the quadrant photodiode and (i) displacement and force measurement calculated from this trajectory using the calibration described in the Methods. The direction and displacement of the bead in panel (g) are consistent with those measured from the trajectory in panel (h).*

As explained in the Methods (Section 2.2.6), for the quantitative analysis, we draw an annulus on the fluorescence image of the bead that encompasses the focal adhesion regions. Fig. 4e shows this annular region for this particular bead at time t = 5 min, and Fig 4f shows the corresponding polar plot of the AA intensity as a function of time. Once we have manually defined the annulus around the bead on the two images at t=0 and t=5 min, we verified that the bead displacement was linear for images at intermediate times (see Fig 4g with the spatial location of the annulus on all 5 images in the xy plane, showing both amplitude and direction of motion). This measurement of the displacement has been used in all our subsequent analyses. Its precision is limited by the camera pixel size (26nm in the sample plane). The displacement deduced from the QPD signal, as shown in Fig 4h, agrees with the amplitude and direction of motion extracted from the fluorescence images. Even though the QPD signal should give us a continuous and more precise measurement of the displacement, transient parasitic fringes in the reflected laser spot recorded on the QPD made it more reliable to use the displacement value extracted from the fluorescence images.

3.3. Analysis on multiple beads

3.3.1. Initial conditions

We analyzed the initial intensity and FRET efficiency for the focal adhesions observed on the different beads before applying the laser force. A scatter plot of the initial FRET efficiency values (Fig. 5) plotted against the initial mVenus intensity (AA channel), shows that initially, FRET efficiencies cover all the tension sensor's range : from high efficiency around 30% where vinculin is not under tension down to 15% where vinculin is subjected to high stretch. The initial FRET efficiency is not correlated (R^2=0.027, p=0.29) with the initial AA intensity (colors indicate the laser trap stiffness that will later on be applied on each bead).

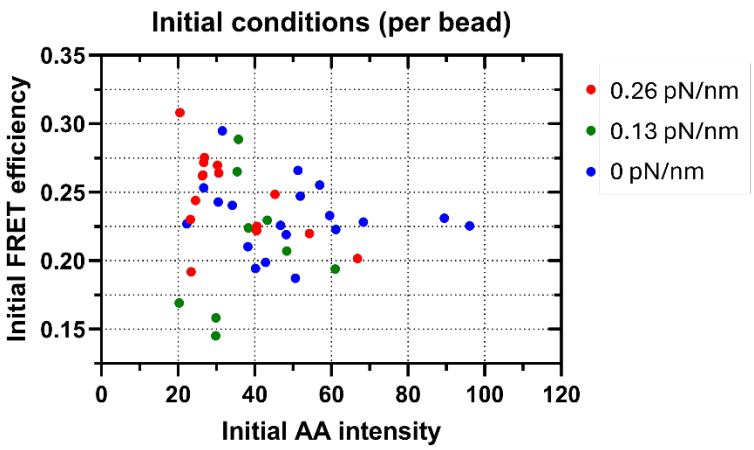

Figure 5 : *Initial FRET efficiencies vs AA intensities before turning on the laser trap. Each dot represents the mean value of the focal adhesions around a given bead. Colors indicate the laser trap stiffness that will later on be applied on each bead, Blue: no laser, Green: 0.13 pN/nm, Red: 0.26 pN/nm*.

3.3.2. Analysis over time

The measurements depicted in Fig. 4 were applied to multiple beads subjected to 3 trapping conditions: a strong trapping k=0.26 pN/nm (15 beads), a medium trapping k = 0.13 pN/nm (9 beads) and no trapping (19 beads). Fig. 6 depicts the change in AA intensity normalized to the value at t=1min (Fig. 6a) and the difference in FRET efficiency compared to t= 1min (Fig. 6b) as a function of time. At t= 5 min, the mean normalized intensity when the laser is on, at both low and high trap stiffness, is larger than the normalized intensity when the laser is off (Fig. 6a). At t= 5 min, the FRET

efficiency decreases on average by 0.016 at 0.26 pN/nm and by 0.012 at 0.13 pN/nm but for both trap stiffnesses, these mean FRET efficiency differences attained at t= 5 min are not significantly different from no trapping. The FRET efficiency difference between t= 5 min and t= 1min, showed no correlation with the initial FRET efficiency (Figure S6).

To analyze the rate of change of AA intensity and FRET efficiency as a function of time and trap stiffness, a simple linear regression was applied to the data in Figs 6a and 6b. In the case of intensity, the regression yields a significant ($p<0.0002$) non-zero positive slope at both low (green in Fig. 6c) and high (red in Fig. 6c) trap stiffness and a negative slope when no laser is present (blue in Fig. 6c). The rate of AA intensity increase is 5.7 times higher at 0.26 pN/nm than at 0.13 pN/nm ($p<0.0001$). The linear regression applied to the FRET efficiency difference reveals a non-zero negative slope in the absence of the trapping laser, and a further decrease when the trapping laser is on. The rate of FRET efficiency decrease is 1.6 times higher at higher stiffness compared with low trap stiffness ($p<0.05$) and 2.2 times higher than the no laser condition ($p<0.001$). However, given the variance in the data, these rates lead to mean decreases in FRET efficiency which are not significantly different after 5 min of optical trapping (Fig. 6b).

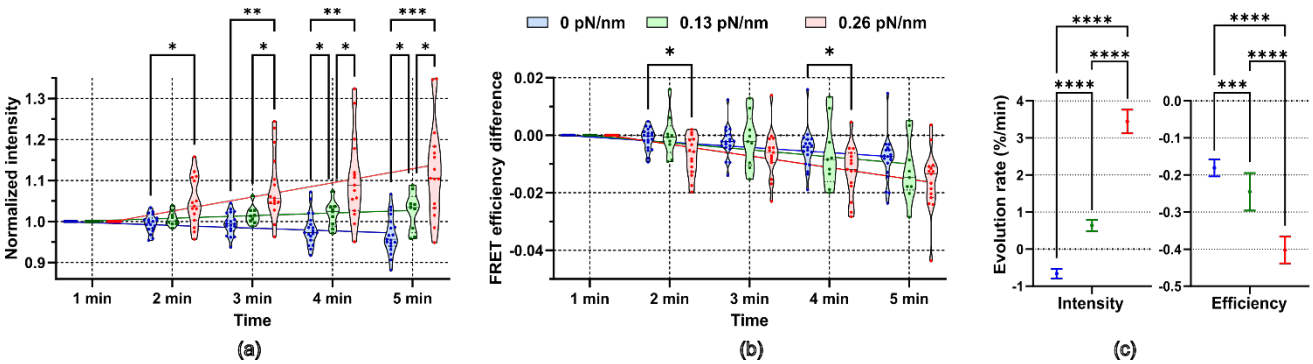

Figure 6 : *Violin plots of AA intensities normalized to t= 1min (a) and of FRET efficiency differences compared to t= 1min (b) as a function of time. Each point represents the mean value of the focal adhesions around a given bead. The data are reported for beads with no trapping (blue points), medium trapping (green points, k=0.13 pN/nm) or strong trapping (red points, k=0.26 pN/nm). t= 1min represents 1 min after the trapping laser is turned on. The lines are linear regressions of intensities and efficiencies versus time with a constraint to pass through the point (1,1) for intensity or (1,0) for FRET efficiency. Significant differences between the different groups are denoted by * (p<0.05), ** (p< 0.01), and *** (p<0.001) (Two-way ANOVA with repeated measures followed by Tukey's multiple comparisons test) (c) Intensity slopes obtained from the linear regressions are respectively (% change/min) -0.7 ± 0.2, 0.6 ± 0.2 and 3.4 ± 0.3 for the different trap stiffnesses; the slopes of the FRET efficiency differences are respectively (difference in % absolute FRET efficiency/min) -0.18 ± 0.03, -0.25 ± 0.05 and -0.40 ± 0.04. All 6 slopes were significantly different from zero (p<0.0002). Significant differences between the slopes are denoted by *** (p<0.001) and **** (p<0.0001) (One-way ANOVA followed by Tukey's multiple comparisons).*

3.4. Intensity and FRET efficiency as a function of laser force

The bead displacement at 5min (Fig. 7a) was used to calculate the force experienced by the bead at 5min using the calibrated trap stiffness. This analysis was used to investigate the relationship between vinculin intensity and vinculin tension as a function of force at the 5 min timepoint. The median displacement remained around 200nm (corresponding to a speed of ~40 nm/min) whether there was no laser trap (207 ± 161 nm), medium trap stiffness (178 ± 338 nm) or high trap stiffness (199 ± 173 nm). The measured forces experienced by individual beads at t= 5 min vary between 8 pN

and 90 pN when the optical trap is on, with the larger forces (>50pN) reached at the higher trap stiffness. However, the largest forces experienced at t= 5 min are not necessarily associated with the largest increases in vinculin recruitment, and relative increases in vinculin intensity above 1.1 could be observed at high laser trap stiffness but at moderate forces between 20 pN and 30 pN (Fig. 7b). Vinculin recruitment appears to depend more on stiffness (red points vs green points in Fig. 7b) than on force. By comparison, the decrease in FRET efficiency observed at t= 5 min, and thus the vinculin tension, does not appear to be correlated with the force reached at 5 min nor with the trap stiffness (Fig. 7c). Here we plotted the FRET efficiency normalized to t=1min rather than the FRET efficiency difference as in Fig. 6b to show that the relative change in intensity can be up to 35% while the relative change in FRET efficiency is only 15% at most.

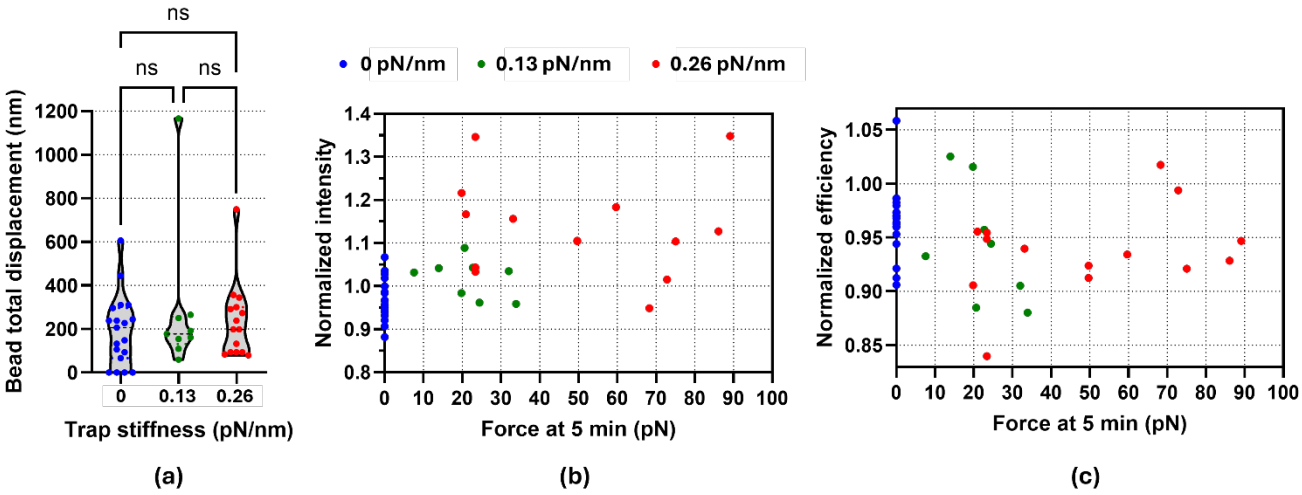

Figure 7 *: (a) Displacement of the beads from their initial positions to their positions at time t=5 min for different trap stiffnesses. No significant difference was found between the different groups (Ordinary one-way ANOVA followed by Tukey's multiple comparisons test). (b) and (c) Normalized AA intensities and FRET efficiencies of the focal adhesions around each bead as function of the force applied by the laser on the bead after 5 min. The beads displaced by more than 500nm are not shown on these force plots since they are not in the linear domain of the trap. Blue points are the beads without laser trapping, green are medium trap stiffness and red high trap stiffness.*

3.5. Intensity increase and FRET efficiency difference correlate at higher stiffness

To further elucidate the effect of trap stiffness, we plotted the AA normalized intensity as a function of FRET efficiency difference (Fig.8) at all times between 1 and 5 min, with color indicating the trap stiffness. This plot is separated in four quadrants corresponding to different trends in the evolution of focal adhesions. In the upper right quadrant, intensity and FRET efficiency increase, which correspond to more vinculin recruited with less tension on each one, a trend that has been associated in the literature with assembling adhesions (53). In the lower right quadrant, vinculin intensity decreases while tension increases, a behavior associated with disassembling adhesions. The lower left quadrant where both intensity and FRET efficiency decrease and where most data points with no laser are located, could be interpreted as an effect of photobleaching by the LED. However, the decrease in AA intensity observed for VinTS (Fig. 8 lower-left quadrant) is lower than the decrease in AA intensity expected in a 12s exposure based on the photobleaching rate of diffuse mVenus in the cytoplasm ($t_{1/2}$= 40s Fig. S1). Finally, in the upper left quadrant, where most of our data points at higher stiffness are located, vinculin intensity increases while FRET efficiency decreases, corresponding to more vinculin accompanied by higher vinculin tension. In addition to this trend,

these data reveal a significant correlation between the increase in vinculin intensity and the decrease in FRET efficiency at 0.26 pN/nm (linear regression R^2=0.38, p<0.0001) compared with no correlation at 0.13 pN/nm (R^2=0.07, p=0.08) or with no laser trap (R^2=0.002, p=0.65).

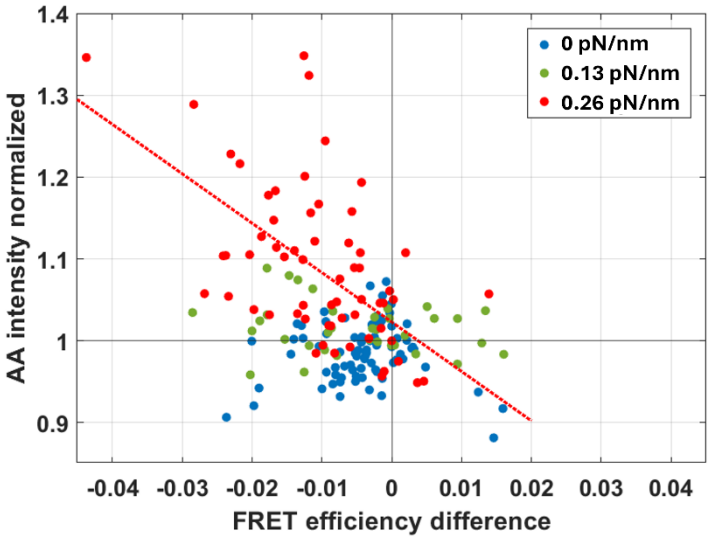

Figure 8 *: Normalized AA intensities of the focal adhesions around each bead as function of FRET efficiency difference plotted for all time points. Blue points are the beads without laser trapping, green are medium trap stiffness and red high trap stiffness. Black lines indicate the areas where normalized intensity increases (above 1) and FRET decreases (left of 0). The red dotted line is the linear regression among the red points subjected to higher trap stiffness (R^2 = 0.38, slope significantly non-zero p-value<0.0001).*

The possible effect of photobleaching attributed to the lower left quadrant of Fig. 8, is difficult to gauge since vinculin turnover can compensate for the effect of photobleaching on vinculin intensity. While the effect of photobleaching can be mitigated by judiciously setting the LED excitation power levels based on the half-life of the fluorophores, photobleaching cannot be completely eliminated. Still, photobleaching alone cannot explain the differences in the results observed at the different trap stiffnesses, as the same LED power and exposure time were maintained in all these experiments.

3.6. Focal adhesions moving away from beads

The vinculin puncta which formed around the beads typically remained on the surface of the bead and moved together with the beads at a speed of ~40 nm/min (Fig. 7a). In addition, the focal adhesions on a given bead experienced similar changes in vinculin intensity or FRET efficiency, justifying their averaging for a given bead (data in Figs. 6-8). However, a few focal adhesions behaved very differently. An example is shown in Fig. 9, where we recorded the FRET images over 11min. In this case, the bead moves to the left, in the negative x-direction at 46nm/min and the two vinculin puncta on the left of the bead (numbered 1 and 4, Fig. 9c) move to the left with the bead and remain on the bead's surface. However, the vinculin puncta on the right (numbered 2 and 3, Fig. 9c) move to the right and away from the bead's surface at higher speeds of 177 nm/min (adhesion 2) and 185 nm/min (adhesion 3). Vinculin intensity for adhesions 1 and 4 remains constant for 7min but slightly decreases over the 11min. On the contrary, intensity of adhesions 2 and 3 increases up to 7min and then remains constant. The vinculin FRET efficiency of adhesions 1 and 4 starts at about 0.28 and decreases by 0.02 over the first 5 minutes then remains constant except for a brief jump at t=10min, while the FRET efficiency of the faster moving adhesions 2 and 3 continues to decrease as they move away from the bead, suggesting that vinculin is experiencing higher tension as it is getting pulled to

the right. We observed such vinculin puncta moving away from the bead's surface in 3 other beads tested at 0.26 pN/nm over 5 min.

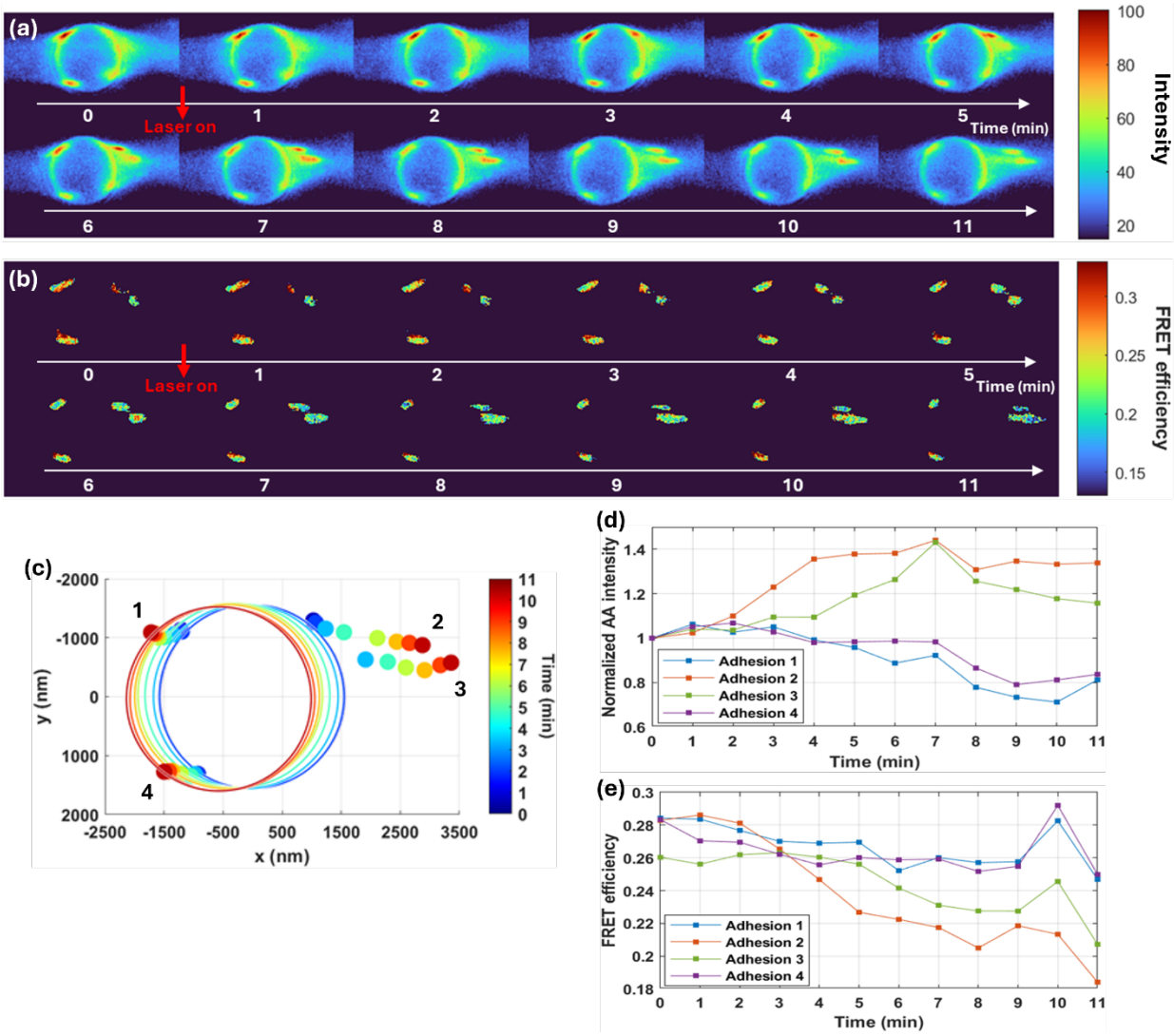

Figure 9 *: Example of focal adhesions moving away from a bead trapped with high stiffness (0.26 pN/nm). (a) and (b) are respectively total intensity (sum AA+DD+DA) and FRET efficiency images of the focal adhesions around the bead. The procedure described in Fig. 4 was used but images were recorded over 11 min. (c) Successive positions of the bead (large circles) and of the four focal adhesions (dots 1, 2, 3, 4). (d) and (e) are the normalized AA intensity and absolute FRET efficiency of each focal adhesion vs time. The bead and two adhesions (1 and 4) move to the left at a speed of 46 nm/min while adhesions 2 and 3 are moving to the right at 177 nm/min (adhesion 2) and 185 nm/min (adhesion 3).*

4. Discussion

To quantify the response of vinculin to a local mechanical stimulus, we developed a microscope which combines optical tweezers and FRET efficiency measurements of the vinculin tension sensor, VinTS. By functionalizing the surface of polystyrene beads with fibronectin, which can attach to integrins at the cell surface, we were able to measure the force imparted to the beads by the cell while quantifying vinculin recruitment and tension at the focal adhesions formed on the beads' surface. We observed the beads as they were displaced by the cell. The direction of this displacement

and its associated force are controlled by the cell. The presence of the optical trap on a bead counteracts the bead's movement and allows us to measure the cell force as a function of increasing laser power (optical trap stiffness). Beads, 3µm in diameter, were tested with trap stiffnesses of 0.26 pN/nm or 0.13 pN/nm or with no trapping laser.

Over the course of 5 min, the median bead displacement was on the order of 200nm and did not depend on trap stiffness with 8-35pN forces reached at 0.13 pN/nm and 20-90pN at 0.26 pN/nm (Fig. 7). After 5 min of optical trapping, both VinTS intensity and tension increased. Both the increase in intensity and rate of intensity increase were significantly higher at 0.26 pN/nm compared with 0.13 pN/nm (Figs. 6a, 6c). The rate of FRET efficiency decrease was faster at 0.26 pN/nm compared with 0.13 pN/nm (Fig. 6c). However, the rates of FRET efficiency decrease were low compared to the rates of intensity increase and the mean FRET efficiency decrease attained at t= 5 min for both trap stiffnesses (decrease by 1-2% in absolute efficiency) was not significantly different from the mean FRET efficiency decrease in the absence of the laser trap (Fig. 6b). Thus, the adhesion response involved an increase in vinculin tension accompanied by a moderate increase in vinculin recruitment (<10% intensity increase) at the lower 0.13 pN/nm trap stiffness while at 0.26 pN/nm, a similar increase in vinculin tension was accompanied by a significantly larger increase in vinculin recruitment (up to 35% intensity increase). In the absence of the laser trap, the decrease in FRET efficiency was accompanied by an average slight decrease (<5%) in vinculin intensity.

The increased vinculin recruitment observed at higher stiffness could not be fully accounted for by the larger magnitude of the cell forces reached at t= 5 min since both high (>50pN) and moderate (20-30 pN) forces could be associated with high vinculin recruitment (>1.1) (Fig. 7b). Instead, our data revealed a correlation between the increase in vinculin intensity and the decrease in FRET efficiency at 0.26 pN/nm that was not observed at 0.13 pN/nm or without laser (Fig. 8). This behavior is different from the relationship between vinculin intensity and tension observed as a function of time during focal adhesion assembly or disassembly (53). Indeed, during assembly, the total vinculin signal increases while vinculin tension starts high and subsequently decreases, and during disassembly, the total vinculin signal decreases while vinculin tension remains low or further decreases. Static measurements of vinculin intensity, such as the initial values reported in Fig. 5, were not correlated with FRET efficiency, corroborating published data showing that VinTS intensity is generally not correlated with FRET efficiency at focal adhesions in various states of assembly or disassembly (21). In this context, our experiments, which are conducted on adhesions in different initial states, demonstrate that a positive correlation between vinculin recruitment and vinculin tension can be induced by the applied external laser force over time. Further study of adhesion dynamics is required to elucidate the mechanisms underlying the interplay between vinculin tension and recruitment in response to sustained external forces.

In the case of 4 beads tested at 0.26 pN/nm, we observed vinculin puncta moving away from the trapped bead. An example in which the movement was in the direction opposite to the bead's displacement was shown in Fig. 9. The moving puncta exhibited both an increase in vinculin intensity and an increase in vinculin tension (decrease in FRET efficiency) (Fig. 9). This suggests that we are not observing a focal adhesion disassembly with disengagement of vinculin. Moving focal adhesions have been previously observed during fibronectin assembly (66,67). The reported speed of those adhesions driven by actin stress fibers (66) was 6.4µm/h, which is approximately half the movement speed we observed in Fig. 9 (~0.18µm/min, which gives ~11µm/h). Future studies with additional labels for paxillin, actin, fibronectin and other components of the focal adhesion complex are required to fully interpret the mechanism leading to the flow of vinculin away from the bead in response to force.

Adhesion maturation and reinforcement was previously observed on fibronectin functionalized beads attached to cells and placed in an optical trap as evidenced by adhesion growth and vinculin recruitment (35-37). The forces measured in this study are comparable to reported values for fibronectin-coated 4.5 µm beads in an optical trap with 0.16 pN/nm stiffness (35,37). The reported retrograde displacement for the 4.5 µm beads was ~450 nm after 5 min for primary chicken fibroblasts and ~180 nm for mouse embryonic fibroblasts (37) which is on the same order as the bead displacement around 200nm per 5 min measured here. However, in other experiments on mouse embryonic fibroblasts involving smaller beads, displacements of ~100nm/s were reported for fibronectin-coated 1µm beads in a 0.4pN/nm optical trap (36) and actin flow without the addition of functionalized beads is typically on the order of 5nm to several tens of nanometers per second at focal adhesions formed on a rigid substrate (25,51,52,68,69). Speeds of ~3µm/min (70) or ~0.5µm/min (71) were also reported in early studies on the retrograde movement of 0.2µm- 1µm sized particles on the membrane of living cells. Assuming the bead movement is governed by actin flow, which is supported by the detection of actin fibers ending at the adhesion complexes forming around the beads (Fig. 3) and previous literature (5), the comparatively low speed of bead displacement measured for the 3µm beads in our study, or the reported 4.5 µm beads (35,37), suggests that actin flow speed may be slowed by the larger bead size. Furthermore, despite the increase in vinculin recruitment, the bead displacement in our data did not change as a function of laser trap stiffness as might be expected from the molecular clutch model (5,24,25,32,55). This may be a consequence of the slow bead displacement and the slow loading rates involved in our experiments. Loading rates could be increased in future studies by using smaller beads. This would increase trap stiffness and potentially increase bead displacement speed. Future studies combining active control of the optical trap in conjunction with the vinculin tension sensor may also allow us to investigate different loading conditions.

5. Conclusion

In summary, our results demonstrate how combining the optical tweezers with the vinculin tension sensor enables dynamic observation and analysis of the interplay between vinculin recruitment and vinculin tension in response to force. Future work shall include the use of vinculin mutants to further elucidate the molecular mechanisms underlying our observations; for example, by altering specific vinculin properties including mutations which affect actin binding (17), the autoinhibitory interaction between vinculin's head and tail domains (15-17) or dimerization of the vinculin tail which allows actin bundling (19). Mutants of the vinculin tension probe specifically altering the directional catch bond between vinculin and actin (72) could provide additional insight. Finally, labeling other proteins such as actin, talin or paxillin, and modulating myosin II- dependent contractility in conjunction with our measurements would help put our work in the context of previous studies on the role of actin stress fibers (43,51) and acto-myosin contractility (26,34) in focal adhesion maturation.

Data availability

The raw data supporting the conclusions of this article and the code used for data analysis in this publication will be shared upon reasonable request to the authors.

Author Contributions

C.D. performed the experiments and analyzed the data both in Palaiseau and in Rutgers. R.I.C. prepared the lentivirus and the transduced fibroblasts expressing VinTS. N.N.B., and N.W. assisted with data analysis. C.D., R.I.C., N.N.B. and N.W. wrote the paper.

Declaration of interests

C.D., NW. and N.N.B. declare no competing interests. R.I.C. is currently employed at The Well Bioscience Inc.

Acknowledgements

We thank Prof. Marie Erard (Univ Paris-Saclay) for help in transfection of the fibroblast cells with VinTS before we could create the lentivirus transduced cells. We thank Prof. Brenton Hoffman (Duke University) for the pRRL-VinTS plasmid and for pertinent discussions. CD was supported by a PhD grant from the French Ministry of Higher Education through the Ecole Doctorale EDOM, plus financial support from Laboratoire Charles Fabry for her missions at Rutgers. This work was supported by Centre National de la Recherche Scientifique (CNRS) through a Tremplin@INP2020 grant, by a grant "Investissements d'Avenir" of the LabEx PALM (N° ANR-10-LABX-0039-PALM) and by a grant part of the France 2030 program (N° ANR-11-IDEX-0003) to N.W. and by NSF award CMMI-1825433 and a Rutgers Global International Collaborative Research Grant to N.N.B.

Supporting Citations

References (73-77) appear in the supplemental material and methods.

References

1. Jaalouk, D. E., and J. Lammerding. 2009. Mechanotransduction gone awry. *Nature Reviews Molecular Cell Biology*. 10(1):63-73, doi: 10.1038/nrm2597.
2. Orr, A. W., B. P. Helmke, B. R. Blackman, and M. A. Schwartz. 2006. Mechanisms of mechanotransduction. *Developmental Cell*. 10(1):11-20, doi: 10.1016/j.devcel.2005.12.006.
3. Gkretsi, V., and T. Stylianopoulos. 2018. Cell Adhesion and Matrix Stiffness: Coordinating Cancer Cell invasion and Metastasis. *Frontiers in Oncology*. 8:145, 145, doi: 10.3389/fonc.2018.00145.
4. Bertocchi, C., Y. Wang, A. Ravasio, Y. Hara, Y. Wu, T. Sailov, M. A. Baird, M. W. Davidson, R. Zaidel-Bar, Y. Toyama, B. Ladoux, R. M. Mege, and P. Kanchanawong. 2017. Nanoscale architecture of cadherin-based cell adhesions. *Nature Cell Biology*. 19(1):28-37, doi: 10.1038/ncb3456.
5. Case, L. B., and C. M. Waterman. 2015. Integration of actin dynamics and cell adhesion by a three-dimensional, mechanosensitive molecular clutch. *Nature Cell Biology*. 17(8):955-963, doi: 10.1038/ncb3191.
6. Kanchanawong, P., G. Shtengel, A. M. Pasapera, E. B. Ramko, M. W. Davidson, H. F. Hess, and C. M. Waterman. 2010. Nanoscale architecture of integrin-based cell adhesions. *Nature*. 468(7323):580-U262, doi: 10.1038/nature09621.

7. Leckband, D. E., and J. de Rooij. 2014. Cadherin Adhesion and Mechanotransduction. *Annual Review of Cell and Developmental Biology*, 30:291-315, doi: 10.1146/annurev-cellbio-100913-013212.
8. Kanchanawong, P., and D. A. Calderwood. 2023. Organization, dynamics and mechanoregulation of integrin-mediated cell-ECM adhesions. *Nature Reviews Molecular Cell Biology*. 24(2):142-161, doi: 10.1038/s41580-022-00531-5.
9. Zaidel-Bar, R. 2013. Cadherin adhesome at a glance. *Journal of Cell Science*. 126(2):373-378, doi: 10.1242/jcs.111559.
10. Zaidel-Bar, R., S. Itzkovitz, A. Ma'ayan, R. Iyengar, and B. Geiger. 2007. Functional atlas of the integrin adhesome. *Nature Cell Biology*. 9(8):858-868, doi: 10.1038/ncb0807-858.
11. Bays, J. L., and K. A. DeMali. 2017. Vinculin in cell-cell and cell-matrix adhesions. *Cellular and Molecular Life Sciences*. 74(16):2999-3009, doi: 10.1007/s00018-017-2511-3.
12. del Rio, A., R. Perez-Jimenez, R. C. Liu, P. Roca-Cusachs, J. M. Fernandez, and M. P. Sheetz. 2009. Stretching Single Talin Rod Molecules Activates Vinculin Binding. *Science*. 323(5914):638-641, doi: 10.1126/science.1162912.
13. Yao, M. X., W. Qiu, R. C. Liu, A. K. Efremov, P. W. Cong, R. Seddiki, M. Payre, C. T. Lim, B. Ladoux, R. M. Mege, and J. Yan. 2014. Force-dependent conformational switch of alpha-catenin controls vinculin binding. *Nature Communications*. 5:4525, 4525, doi: 10.1038/ncomms5525.
14. Carisey, A., R. Tsang, A. M. Greiner, N. Nijenhuis, N. Heath, A. Nazgiewicz, R. Kemkemer, B. Derby, J. Spatz, and C. Ballestrem. 2013. Vinculin Regulates the Recruitment and Release of Core Focal Adhesion Proteins in a Force-Dependent Manner. *Current Biology*. 23(4):271-281, doi: 10.1016/j.cub.2013.01.009.
15. Johnson, R. P., and S. W. Craig. 1994. An intramolecular association between the head and tail domains of vinculin modulates talin binding. *Journal of Biological Chemistry*. 269(17):12611-12619, doi:10.1016/S0021-9258(18)99920-S.
16. Johnson, R. P., and S. W. Craig. 1995. F-actin binding site masked by the intramolecular association of vinculin head and tail domains. *Nature*. 373(6511):261-264, doi: 10.1038/373261a0.
17. Thompson, P. M., C. E. Tolbert, K. Shen, P. Kota, S. M. Palmer, K. M. Plevock, A. Orlova, V. E. Galkin, K. Burridge, E. H. Egelman, N. V. Dokholyan, R. Superfine, and S. L. Campbell. 2014. Identification of an Actin Binding Surface on Vinculin that Mediates Mechanical Cell and Focal Adhesion Properties. *Structure*. 22(5):697-706, doi: 10.1016/j.str.2014.03.002.
18. Johnson, R. P., and S. W. Craig. 2000. Actin activates a cryptic dimerization potential of the vinculin tail domain. *Journal of Biological Chemistry*. 275(1):95-105, doi: 10.1074/jbc.275.1.95.
19. Kim, L. Y., P. M. Thompson, H. T. Lee, M. Pershad, S. L. Campbell, and G. M. Alushin. 2016. The Structural Basis of Actin Organization by Vinculin and Metavinculin. *Journal of Molecular Biology*. 428(1):10-25, doi: 10.1016/j.jmb.2015.09.031.
20. Shen, K., C. E. Tolbert, C. Guilluy, V. S. Swaminathan, M. E. Berginski, K. Burridge, R. Superfine, and S. L. Campbell. 2011. The Vinculin C-terminal Hairpin Mediates F-actin Bundle Formation, Focal Adhesion, and Cell Mechanical Properties. *Journal of Biological Chemistry*. 286(52):45103-45115, doi: 10.1074/jbc.m111.244293.
21. Tao, A., A. S. LaCroix, T. C. Shoyer, V. Venkatraman, K. L. Xu, B. Feiger, and B. D. Hoffman. 2023. Identifying constitutive and context-specific molecular-tension-sensitive protein recruitment within focal adhesions. *Developmental Cell*. 58(6):522-534, doi: 10.1016/j.devcel.2023.02.015.

22. Kuo, J. C., X. M. Han, C. T. Hsiao, J. R. Yates, and C. M. Waterman. 2011. Analysis of the myosin-II-responsive focal adhesion proteome reveals a role for β-Pix in negative regulation of focal adhesion maturation. *Nature Cell Biology*. 13(4):383-393, doi: 10.1038/ncb2216.
23. Balaban, N. Q., U. S. Schwarz, D. Riveline, P. Goichberg, G. Tzur, I. Sabanay, D. Mahalu, S. Safran, A. Bershadsky, L. Addadi, and B. Geiger. 2001. Force and focal adhesion assembly: a close relationship studied using elastic micropatterned substrates. *Nature Cell Biology*. 3(5):466-472, doi: 10.1038/35074532.
24. Chan, C. E., and D. J. Odde. 2008. Traction Dynamics of Filopodia on Compliant Substrates. *Science*. 322(5908):1687-1691, doi: 10.1126/science.1163595
25. Elosegui-Artola, A., R. Oria, Y. Chen, A. Kosmalska, C. Pérez-González, N. Castro, C. Zhu, X. Trepat, and P. Roca-Cusachs. 2016. Mechanical regulation of a molecular clutch defines force transmission and transduction in response to matrix rigidity. *Nature Cell Biology*. 18(5):540-548, doi: 10.1038/ncb3336.
26. Pasapera, A. M., I. C. Schneider, E. Rericha, D. D. Schlaepfer, and C. M. Waterman. 2010. Myosin II activity regulates vinculin recruitment to focal adhesions through FAK-mediated paxillin phosphorylation. *Journal of Cell Biology*. 188(6):877-890, doi: 10.1083/jcb.200906012.
27. Pelham, R. J., and Y. L. Wang. 1997. Cell locomotion and focal adhesions are regulated by substrate flexibility. *Proceedings of the National Academy of Sciences of the United States of America*. 94(25):13661-13665, doi: 10.1073/pnas.94.25.13661.
28. Plotnikov, S., A. Pasapera, B. Sabass, and C. M. Waterman. 2012. Force Fluctuations within Focal Adhesions Mediate ECM-Rigidity Sensing to Guide Directed Cell Migration. *Cell*. 151(7):1513-1527, doi: 10.1016/j.cell.2012.11.034.
29. Yamashita, H., T. Ichikawa, D. Matsuyama, Y. Kimura, K. Ueda, S. W. Craig, I. Harada, and N. Kioka. 2014. Interaction of the vinculin proline-rich linker region with vinexin α in sensing extracellular matrix stiffness. *Journal of Cell Science*. 127(9):1875-1886, doi: 10.1242/jcs.133645.
30. Zhou, D. W., T. T. Lee, S. Weng, J. Fu, and A. J. García. 2017. Effects of substrate stiffness and actomyosin contractility on coupling between force transmission and vinculin–paxillin recruitment at single focal adhesions. *Molecular Biology of the Cell*. 28(14):1901-1911, doi: 10.1091/mbc.e17-02-0116.
31. Prager-Khoutorsky, M., A. Lichtenstein, R. Krishnan, K. Rajendran, A. Mayo, Z. Kam, B. Geiger, and A. D. Bershadsky. 2011. Fibroblast polarization is a matrix-rigidity-dependent process controlled by focal adhesion mechanosensing. *Nature Cell Biology*. 13(12):1457-1465, doi: 10.1038/ncb2370.
32. Andreu, I., B. Falcones, S. Hurst, N. Chahare, X. Quiroga, A.-L. Le Roux, Z. Kechagia, A. E. M. Beedle, A. Elosegui-Artola, X. Trepat, R. Farré, T. Betz, I. Almendros, and P. Roca-Cusachs. 2021. The force loading rate drives cell mechanosensing through both reinforcement and cytoskeletal softening. *Nature Communications*. 12(1):4229, doi: 10.1038/s41467-021-24383-3.
33. Dessalles, C. A., C. Leclech, A. Castagnino, and A. I. Barakat. 2021. Integration of substrate- and flow-derived stresses in endothelial cell mechanobiology. *Communications Biology*. 4(1):764 doi: 10.1038/s42003-021-02285-w.
34. Riveline, D., E. Zamir, N. Q. Balaban, U. S. Schwarz, T. Ishizaki, S. Narumiya, Z. Kam, B. Geiger, and A. D. Bershadsky. 2001. Focal contacts as mechanosensors: Externally applied local mechanical force induces growth of focal contacts by an mDia1-dependent and ROCK-

independent mechanism. *Journal of Cell Biology*. 153(6):1175-1185, doi: 10.1083/jcb.153.6.1175.
35. Baumann, H., M. Schwingel, M. Sestu, A. Burcza, S. Marg, W. Ziegler, A. V. Taubenberger, D. J. Muller, M. Bastmeyer, and C. M. Franz. 2023. Biphasic reinforcement of nascent adhesions by vinculin. *Journal of Molecular Recognition*.36:e3012, doi: 10.1002/jmr.3012.
36. Galbraith, C. G., K. M. Yamada, and M. P. Sheetz. 2002. The relationship between force and focal complex development. *Journal of Cell Biology*. 159(4):695-705, doi: 10.1083/jcb.200204153.
37. Schwingel, M., and M. Bastmeyer. 2013. Force Mapping during the Formation and Maturation of Cell Adhesion Sites with Multiple Optical Tweezers. *Plos One*. 8(1):e54850, e54850, doi: 10.1371/journal.pone.0054850.
38. Stilgoe, A. B., I. A. Favre-Bulle, M. L. Watson, V. Gomez-Godinez, M. W. Berns, D. Preece, and H. Rubinsztein-Dunlop. 2024. Shining Light in Mechanobiology: Optical Tweezers, Scissors, and Beyond. *Acs Photonics*. 11(3):917-940, doi: 10.1021/acsphotonics.4c00064.
39. Wang, Y. X., E. L. Botvinick, Y. H. Zhao, M. W. Berns, S. Usami, R. Y. Tsien, and S. Chien. 2005. Visualizing the mechanical activation of Src. *Nature*. 434(7036):1040-1045, doi: 10.1038/nature03469.
40. Fass, J. N., and D. J. Odde. 2003. Tensile force-dependent neurite elicitation via anti-β1 integrin antibody-coated magnetic beads. *Biophysical Journal*. 85(1):623-636, doi: 10.1016/s0006-3495(03)74506-8.
41. Dumbauld, D. W., T. T. Lee, A. Singh, J. Scrimgeour, C. A. Gersbach, E. A. Zamir, J. P. Fu, C. S. Chen, J. E. Curtis, S. W. Craig, and A. J. García. 2013. How vinculin regulates force transmission. *Proceedings of the National Academy of Sciences of the United States of America*. 110(24):9788-9793, doi: 10.1073/pnas.1216209110.
42. Katsuta, H., S. Okuda, K. Nagayama, H. Machiyama, S. Kidoaki, M. Kato, M. Sokabe, T. Miyata, and H. Hirata. 2023. Actin crosslinking by α-actinin averts viscous dissipation of myosin force transmission in stress fibers. *Iscience*. 26(3):106090, doi: 10.1016/j.isci.2023.106090.
43. Oakes, P. W., Y. Beckham, J. Stricker, and M. L. Gardel. 2012. Tension is required but not sufficient for focal adhesion maturation without a stress fiber template. *Journal of Cell Biology*. 196(3):363-374, doi: 10.1083/jcb.201107042.
44. Legant, W. R., J. S. Miller, B. L. Blakely, D. M. Cohen, G. M. Genin, and C. S. Chen. 2010. Measurement of mechanical tractions exerted by cells in three-dimensional matrices. *Nature Methods*. 7(12):969-U113, doi: 10.1038/nmeth.1531.
45. Sabass, B., M. L. Gardel, C. M. Waterman, and U. S. Schwarz. 2008. High resolution traction force microscopy based on experimental and computational advances. *Biophysical Journal*. 94(1):207-220, doi: 10.1529/biophysj.107.113670.
46. Sarangi, B. R., M. Gupta, B. L. Doss, N. Tissot, F. Lam, R. M. Mège, N. Borghi, and B. Ladoux. 2017. Coordination between Intra- and Extracellular Forces Regulates Focal Adhesion Dynamics. *Nano Letters*. 17(1):399-406, doi: 10.1021/acs.nanolett.6b04364.
47. Tan, J. L., J. Tien, D. M. Pirone, D. S. Gray, K. Bhadriraju, and C. S. Chen. 2003. Cells lying on a bed of microneedles: An approach to isolate mechanical force. *Proceedings of the National Academy of Sciences of the United States of America*. 100(4):1484-1489, doi: 10.1073/pnas.0235407100.
48. Gallant, N. D., K. E. Michael, and A. J. García. 2005. Cell adhesion strengthening:: Contributions of adhesive area, integrin binding, and focal adhesion assembly. *Molecular Biology of the Cell*. 16(9):4329-4340, doi: 10.1091/mbc.E05-02-0170.

49. Stricker, J., Y. Aratyn-Schaus, P. W. Oakes, and M. L. Gardel. 2011. Spatiotemporal Constraints on the Force-Dependent Growth of Focal Adhesions. *Biophysical Journal*. 100(12):2883-2893, doi: 10.1016/j.bpj.2011.05.023.
50. Choquet, D., D. P. Felsenfeld, and M. P. Sheetz. 1997. Extracellular matrix rigidity causes strengthening of integrin-cytoskeleton linkages. *Cell*. 88(1):39-48, doi: 10.1016/s0092-8674(00)81856-5.
51. Gardel, M. L., B. Sabass, L. Ji, G. Danuser, U. S. Schwarz, and C. M. Waterman. 2008. Traction stress in focal adhesions correlates biphasically with actin retrograde flow speed. *The Journal of Cell Biology*. 183(6):999-1005, doi: 10.1083/jcb.200810060.
52. Hu, K., L. Ji, K. T. Applegate, G. Danuser, and C. M. Waterman-Storer. 2007. Differential Transmission of Actin Motion Within Focal Adhesions. *Science*. 315(5808):111-115, doi: 10.1126/science.1135085.
53. Grashoff, C., B. D. Hoffman, M. D. Brenner, R. B. Zhou, M. Parsons, M. T. Yang, M. A. McLean, S. G. Sligar, C. S. Chen, T. Ha, and M. A. Schwartz. 2010. Measuring mechanical tension across vinculin reveals regulation of focal adhesion dynamics. *Nature*. 466(7303):263-U143, doi: 10.1038/nature09198.
54. LaCroix, A. S., A. D. Lynch, M. E. Berginski, and B. D. Hoffman. 2018. Tunable molecular tension sensors reveal extension-based control of vinculin loading. *Elife*. 7:e33927, doi: 10.7554/eLife.33927.
55. Honasoge, K. S., Z. Karagöz, B. T. Goult, H. Wolfenson, V. L. S. Lapointe, and A. Carlier. 2023. Force-dependent focal adhesion assembly and disassembly: A computational study. *PLOS Computational Biology*. 19(10):e1011500, doi: 10.1371/journal.pcbi.1011500.
56. Huang, D. L., N. A. Bax, C. D. Buckley, W. I. Weis, and A. R. Dunn. 2017. Vinculin forms a directionally asymmetric catch bond with F-actin. *Science*. 357(6352):703-706, doi: 10.1126/science.aan2556.
57. Novikova, E. A., and C. Storm. 2021. Evolving roles and dynamics for catch and slip bonds during adhesion cluster maturation. *Physical Review E*. 103(3):Article 032402, doi: 10.1103/PhysRevE.103.032402.
58. Sergides, M., L. Perego, T. Galgani, C. Arbore, F. S. Pavone, and M. Capitanio. 2021. Probing mechanotransduction in living cells by optical tweezers and FRET-based molecular force microscopy. *European Physical Journal Plus*. 136(3):316, 316, doi: 10.1140/epjp/s13360-021-01273-7.
59. Dubois, C., L. Houel-Renault, M. Erard, N. N. Boustany, and N. Westbrook. 2023. Forster resonance energy transfer efficiency measurements on vinculin tension sensors at focal adhesions using a simple and cost-effective setup. *Journal of Biomedical Optics*. 28(8):082808, 082808, doi: 10.1117/1.Jbo.28.8.082808.
60. Rothenberg, K. E., D. W. Scott, N. Christoforou, and B. D. Hoffman. 2018. Vinculin Force-Sensitive Dynamics at Focal Adhesions Enable Effective Directed Cell Migration. *Biophysical Journal*. 114(7):1680-1694, doi: 10.1016/j.bpj.2018.02.019.
61. Moazzeni, S., K. Kyker-Snowman, R. I. Cohen, H. Wang, R. Li, D. I. Shreiber, J. D. Zahn, Z. Shi, and H. Lin. 2025. N-Cadherin based adhesion and Rac1 activity regulate tension polarization in the actin cortex. *Scientific Reports*. 15(1):4296, 4296, doi: 10.1038/s41598-025-88537-9.
62. Mitta, B., M. Rimann, M. U. Ehrengruber, M. Ehrbar, V. Djonov, J. Kelm, and M. Fussenegger. 2002. Advanced modular self-inactivating lentiviral expression vectors for multigene interventions in mammalian cells and in vivo transduction. *Nucleic Acids Research*. 30(21):e113, e113, doi: 10.1093/nar/gnf112.

63. Counter, C. M., W. C. Hahn, W. Y. Wei, S. D. Caddle, R. L. Beijersbergen, P. M. Lansdorp, J. M. Sedivy, and R. A. Weinberg. 1998. Dissociation among in vitro telomerase activity, telomere maintenance, and cellular immortalization. *Proceedings of the National Academy of Sciences of the United States of America*. 95(25):14723-14728, doi: 10.1073/pnas.95.25.14723.
64. Gillant, F., J. Moreau, M. U. Richly, A. Alexandrou, K. Perronet, and N. Westbrook. 2023. Accurate calibration of optical tweezers close to a glass surface using interference rings in backscattered light. *Journal of the European Optical Society-Rapid Publications*. 19(1):28, 28, doi: 10.1051/jeos/2023026.
65. Schindelin, J., I. Arganda-Carreras, E. Frise, V. Kaynig, M. Longair, T. Pietzsch, S. Preibisch, C. Rueden, S. Saalfeld, B. Schmid, J.-Y. Tinevez, D. J. White, V. Hartenstein, K. Eliceiri, P. Tomancak, and A. Cardona. 2012. Fiji: an open-source platform for biological-image analysis. *Nature Methods*. 9(7):676-682, doi: 10.1038/nmeth.2019.
66. Lu, J. Y., A. D. Doyle, Y. Shinsato, S. H. Wang, M. A. Bodendorfer, M. H. Zheng, and K. M. Yamada. 2020. Basement Membrane Regulates Fibronectin Organization Using Sliding Focal Adhesions Driven by a Contractile Winch. *Developmental Cell*. 52(5):631-+, doi: 10.1016/j.devcel.2020.01.007.
67. Tomer, D., C. Arriagada, S. Munshi, B. E. Alexander, B. French, P. Vedula, V. Caorsi, A. House, M. Guvendiren, A. Kashina, J. E. Schwarzbauer, and S. Astrof. 2022. A new mechanism of fibronectin fibril assembly revealed by live imaging and super-resolution microscopy. *Journal of Cell Science*. 135(16):jcs260120, doi: 10.1242/jcs.260120.
68. Carlsson, A. E. 2010. Actin Dynamics: From Nanoscale to Microscale. *Annual Review of Biophysics*. 39(1):91-110, doi: 10.1146/annurev.biophys.093008.131207.
69. Watanabe, N., and T. J. Mitchison. 2002. Single-molecule speckle analysis of Actin filament turnover in lamellipodia. *Science*. 295(5557):1083-1086, doi: 10.1126/science.1067470.
70. Harris, A., and G. Dunn. 1972. Centripetal transport of attached particles on both surfaces of moving fibroblasts. *Experimental Cell Research*. 73(2):519-523, doi: 10.1016/0014-4827(72)90084-5.
71. Abercrombie, M., J. E. Heaysman, and S. M. Pegrum. 1970. Locomotion of fibroblasts in culture: III. Movements of particles on the dorsal surface of the leading lamella. *Experimental Cell Research*. 62(2-3):389-398, doi: 10.1016/0014-4827(70)90570-7.
72. Chirasani, V. R., M. A. I. Khan, J. N. Malavade, N. V. Dokholyan, B. D. Hoffman, and S. L. Campbell. 2023. Molecular basis and cellular functions of vinculin-actin directional catch bonding. *Nature Communications*. 14(1):8300, doi: 10.1038/s41467-023-43779-x.
73. Boussif, O., F. Lezoualch, M. A. Zanta, M. D. Mergny, D. Scherman, B. Demeneix, and J. P. Behr. 1995. A versatile vector for gene and oligonucleotide transfer into cells in culture and in vivo: polyethylenimine. *Proceedings of the National Academy of Sciences of the United States of America*. 92(16):7297-7301, doi: 10.1073/pnas.92.16.7297.
74. Ellis, B. L., P. R. Potts, and M. H. Porteus. 2011. Creating Higher Titer Lentivirus with Caffeine. *Human Gene Therapy*. 22(1):93-100, doi: 10.1089/hum.2010.068.
75. Cranfill, P. J., B. R. Sell, M. A. Baird, J. R. Allen, Z. Lavagnino, H. M. de Gruiter, G. J. Kremers, M. W. Davidson, A. Ustione, and D. W. Piston. 2016. Quantitative assessment of fluorescent proteins. *Nature Methods*. 13(7):557-562, doi: 10.1038/nmeth.3891.
76. Berg-Sorensen, K., and H. Flyvbjerg. 2004. Power spectrum analysis for optical tweezers. *Review of Scientific Instruments*. 75(3):594-612, doi: 10.1063/1.1645654.
77. Hansen, P. M., I. M. Tolic-Norrelykke, H. Flyvbjerg, and K. Berg-Sorensen. 2006. tweezercalib 2.0: Faster version of MatLab package for precise calibration of optical tweezers. *Computer Physics Communications*. 174(6):518-520, doi: 10.1016/j.cpc.2005.11.007.

78. Pesce, G., P. H. Jones, O. M. Maragò, and G. Volpe. 2020. Optical tweezers: theory and practice. *European Physical Journal Plus*. 135(12):949, 949, doi: 10.1140/epjp/s13360-020-00843-5.